

## Research Article

# Preparation and Photocatalytic Performances of WO<sub>3</sub>/TiO<sub>2</sub> Composite Nanofibers

Xiuping Han <sup>1,2</sup>, Binghua Yao <sup>1</sup>, Keying Li,<sup>1</sup> Wenjing Zhu,<sup>2</sup> and Xuyuan Zhang<sup>3</sup>

<sup>1</sup>*Xi'an University of Technology, Xi'an 710048, China*

<sup>2</sup>*School of Science, Hainan University, Haikou 570228, China*

<sup>3</sup>*Hainan Vocational University of Science and Technology, Haikou 571126, China*

Correspondence should be addressed to Binghua Yao; [bhyao@xaut.edu.cn](mailto:bhyao@xaut.edu.cn)

Received 3 July 2020; Accepted 23 July 2020; Published 30 August 2020

Guest Editor: Tifeng Jiao

Copyright © 2020 Xiuping Han et al. This is an open access article distributed under the Creative Commons Attribution License, which permits unrestricted use, distribution, and reproduction in any medium, provided the original work is properly cited.

The use of sunlight for photocatalytic oxidation is an ideal strategy, but it is limited by factors such as insufficient light absorption intensity of the photocatalyst and easy recombination of photogenerated electron holes. TiO<sub>2</sub> is favored by researchers as an environment-friendly catalyst. In this paper, TiO<sub>2</sub> is combined with WO<sub>3</sub> to obtain a nanofiber with excellent catalytic performance under sunlight. The WO<sub>3</sub>/TiO<sub>2</sub> composite nanofibers were synthesized by using the electrospinning method. The X-ray diffraction (XRD) analysis indicated that WO<sub>3</sub> was successfully integrated onto the surface of TiO<sub>2</sub>. The photodegradation performance and photocurrent analysis of the prepared nanofibers showed that the addition of WO<sub>3</sub> really improved the photocatalytic performance of TiO<sub>2</sub> nanofibers, methylene blue (MB) degradation rate increased from 72% to 96%, and 5% was the optimal composite mole percentage of W to Ti. The scanning electron microscopy (SEM), X-ray photoelectron spectroscopy (XPS), UV-Vis diffuse reflectance spectra (UV-Vis DRS), and Brunauer-Emmett-Teller (BET) analysis further characterized the properties of 5% WO<sub>3</sub>/TiO<sub>2</sub> nanofibers. The H<sub>2</sub> generation rate of 5% WO<sub>3</sub>/TiO<sub>2</sub> nanofibers was 107.15 μmol·g<sup>-1</sup>·h<sup>-1</sup>, in comparison with that of TiO<sub>2</sub> nanofibers (73.21 μmol·g<sup>-1</sup>·h<sup>-1</sup>) under the same condition. The 5% WO<sub>3</sub>/TiO<sub>2</sub> produced ·OH under illumination, which played an important role in the MB degradation. Also, the enhanced photocatalytic mechanism was also proposed based on the detailed analysis of the band gap and the active species trapping experiment. The results indicated that the effective separation of Z-scheme photogenerated electron-hole pairs and transfer system constructed between TiO<sub>2</sub> and WO<sub>3</sub> endowed the excellent photocatalytic activity of 5% WO<sub>3</sub>/TiO<sub>2</sub> nanofibers.

## 1. Introduction

Photocatalytic oxidation is a green, environmentally friendly, inexpensive, and efficient wastewater treatment technology. The efficient degradation of toxic and hazardous substances in wastewater is the goal that researchers have always sought and has achieved very good results. For example, Jiao and coworkers have prepared a series of environmentally friendly composite hydrogel photocatalysts, which can efficiently degrade the toxic and harmful substances nitrophenol and nitroaniline that are difficult to degrade in wastewater [1–3].

The core of photocatalytic oxidation technology is photocatalyst. Since Fujishima reported that TiO<sub>2</sub> would

decompose water under ultraviolet light irradiation in 1972 [4], TiO<sub>2</sub> has attracted considerable attention in photocatalysis because of its superior photocatalytic activity, good chemical stability, nontoxicity, low cost, and no secondary pollution [5]. However, several disadvantages of TiO<sub>2</sub> photocatalyst severely blocked its practical application such as the limited visible light response, low specific surface area, and high recombination efficiency of charge carriers, which lead to the fact that the photocatalytic activity of TiO<sub>2</sub> was relatively unsatisfactory [6]. Numerous efforts such as morphology designing [7], noble metal [8, 9], or nonmetal doping [10], ion doping [11, 12], composite material forming [13, 14], and heterojunction fabricating [15] had been devoted to improving its photocatalytic performance. Among

the abovementioned methods, heterojunction fabricating had been considered as an efficient strategy for broadening spectrum response range and effectively improving the separation efficiency of photogenerated charge carriers. For instance, Li and coworkers [16] fabricated  $\text{TiO}_2/\text{MoS}_2$  nanoheterojunctions by electrospinning and hydrothermal method and demonstrated that as-prepared samples exhibited super photocatalytic hydrogen evolution activity of  $171.24 \mu\text{mol}\cdot\text{g}^{-1}\cdot\text{L}^{-1}$ . Chen et al. [17] also reported that coupling  $\text{LaNiO}_3$  with  $\text{TiO}_2$  would remarkably enhance the photocatalytic activity of  $\text{TiO}_2$  and explained that the heterojunction formed between them played an important role in improving the photocatalytic performance. Recently,  $\text{TiO}_2\text{-C}_3\text{N}_4$  [18],  $\text{CdS}/\text{TiO}_2$  [19],  $\text{TiO}_2/\text{NiO}$  [20], and  $\text{TiO}_2/\text{Cu}_2\text{O}$  [21] had been reported and shown enhanced photocatalytic performance for organic pollutant degradation and  $\text{H}_2$  evaluation.

$\text{WO}_3$  as an n-type semiconductor with an energy band gap of 2.7 eV has also been considered as an efficient candidate for the formation of heterojunction with other photocatalysts due to its excellent physiochemical stability and strong visible light response [22, 23]. Thus, fabricating  $\text{WO}_3$  with  $\text{TiO}_2$  to form heterojunction might be an effective strategy to enhance the photocatalytic performance of  $\text{TiO}_2$ . For example, Pan et al. prepared  $\text{WO}_3$ -coated  $\text{TiO}_2$  catalysts via alcoholthermal synthesis; thus, the  $\text{WO}_3$ -coated  $\text{TiO}_2$  heterostructure exhibited excellent photocatalytic performance compared with anatase  $\text{TiO}_2$  [24]. Hunge et al. synthesized  $\text{WO}_3/\text{TiO}_2$  thin films by the two-step spray pyrolysis method, and because a junction is formed between the  $\text{WO}_3$  and  $\text{TiO}_2$ , their photoelectrocatalytic activity was enhanced [25]. Khan et al. fabricated hybrid  $\text{TiO}_2/\text{WO}_3$  samples, and  $\text{TiO}_2$  and  $\text{WO}_3$  act in synergy effectively separated holes and electrons and improved photocatalytic performance [26].

The photocatalytic performance of the catalyst was closely related to its micromorphology and porous structure. The fibrous photocatalyst had a large specific surface area and more exposed active sites, which ensured its higher adsorption capacity and better photocatalytic activity [27]. Moreover, the special fibrous structure was beneficial to transfer photogenerated electrons and holes from the bulk phase to the catalyst surface and inhibited the recombination of electron-hole pairs. Therefore, fibrous photocatalysts could generate higher photocatalytic performance in comparison with traditional materials [28, 29]. Hu et al. synthesized  $\text{TiO}_2/\text{WO}_3$  nanofibers by electrospinning technique and clarified that the heterojunction formed after the addition of  $\text{WO}_3$  in  $\text{TiO}_2$  fibers increased  $\text{H}_2$  production rate [30]. Gao et al. prepared  $\text{TiO}_2/\text{WO}_3$  nanofibers where the hydrogen production rate is  $27.73 \mu\text{mol}/\text{h}$  and clarified the formation of band bending and artificial Z-scheme when there is a  $\text{WO}_3$  contact with  $\text{TiO}_2$  [31]. Soares and Alves synthesized  $\text{TiO}_2/\text{WO}_3$  fibers by electrospinning which increased the photocatalytic performance due to the addition of  $\text{H}_2\text{WO}_4$  and degraded 51% of the dye in 135 min [32].

In this work, the fibers  $\text{TiO}_2$  and  $\text{WO}_3/\text{TiO}_2$  fibers were successfully synthesized through a one-step electrospinning process and were characterized by using XRD, SEM, XPS,

UV-Vis DRS, and BET techniques. The photocatalytic performance and stability of as-prepared samples were estimated by photocatalytic degradation of MB and hydrogen evolution under UV-Vis light irradiation. Finally, the possible enhanced photocatalytic mechanism of  $\text{WO}_3/\text{TiO}_2$  heterojunction nanofibers was proposed.

## 2. Experimental

**2.1. Synthesis by Electrospinning.** The nanofibers of  $\text{TiO}_2$  were obtained from the precursor solution made by mixing 2.50 g of tetrabutyl titanate, 9.0 mL of glacial acetic acid, 1.10 g of polyvinylpyrrolidone (PVP), and 10 mL of ethanol solution containing N,N-dimethylformamide ( $v:v=1:1$ ) as the solvent. The  $\text{WO}_3/\text{TiO}_2$  precursor solution was prepared by mixing the abovementioned reactants plus different amounts of  $(\text{NH}_4)_2\text{WO}_4$ . These solutions were continuous stirring for 12 h and then transferred into an electrospinning device. The electrospinning parameters were optimized such as flow rate for solution 2.7 mL/h, an applied voltage of 14 kV, and the tip to collector distance of 11 cm. The samples collected on aluminum-foil collectors were designated as precursors.

Finally, the precursors prepared were heated up to  $520^\circ\text{C}$  at a heating rate of  $1^\circ\text{C}/\text{min}$  for four hours in a tube furnace, and the nanofibers of  $\text{TiO}_2$  and  $\text{WO}_3/\text{TiO}_2$  were obtained. We prepared a set of  $\text{WO}_3/\text{TiO}_2$  nanofibers by varying  $(\text{NH}_4)_2\text{WO}_4$  molar percent at 1%, 5%, and 10% where all other parameters remained unchanged.

**2.2. Characterization of As-Prepared Samples.** XRD patterns of samples were collected in the range of  $10\text{--}80^\circ$  using a 6100 X-ray diffract meter with  $\text{Cu K}\alpha$  radiation. The morphologies of photocatalysts were characterized by VTGA3 SBH scanning electron microscopy. XPS analysis was performed using a K-alpha photoelectron spectroscope. UV-Vis DRS of photocatalysts were analyzed by UV-2102, UV-Vis spectrophotometers with  $\text{BaSO}_4$  as the internal reflectance standard. The BET surface area of samples was carried out using the JK-BK122W apparatus. The photocurrent was measured using a CHI-660b electrochemical analyzer.

### 2.3. Evaluation of Photocatalytic Activity

**2.3.1. Photocatalytical Degradation of MB.** The photocatalytic performance was estimated by the degradation of MB and was performed. In a typical process, 50 mg of as-prepared samples was dispersed in 50 mL  $20 \text{mg}\cdot\text{L}^{-1}$  MB and stirred in the dark for 30 min before irradiation to reach the adsorption/desorption equilibrium. Then, the solution was illuminated with a 250 W Xenon lamp. 5 mL of the sample was collected sequentially at every 20 min and then centrifuged, and the supernatant dye solution was analyzed by TU-1901 spectrophotometer at 664 nm. The degradation efficiency was calculated according to the equation of  $D\% = (A_0 - A_t)/A_0 \times 100\%$ .  $A_0$  and  $A_t$  were the were the absorbance of MB at an initial time and time  $t$ , respectively.

**2.3.2. Photocatalytic Hydrogen Evolution.** The photocatalytic hydrogen evolution experiments were carried out by a DS-GHX-V system with a 100 W Mercury lamp as the light source. In short, 30 mg of as-prepared photocatalysts was added to a sealed 100 mL quartz tube containing a mixture of 60 mL of  $0.25 \text{ mol}\cdot\text{L}^{-1}$   $\text{Na}_2\text{S}$  and  $0.35 \text{ mol}\cdot\text{L}^{-1}$   $\text{Na}_2\text{SO}_3$  aqueous solution as a sacrificial agent. Before irradiation, the reaction solution was purged with  $\text{N}_2$  for 30 min to exhaust the air in the quartz tube. The quartz tube was kept in a circulating cooling water system to maintain the temperature at  $25^\circ\text{C}$  and stirred continuously to make an even dispersed solution. A Thermo Trace 1300 gas chromatograph equipped was adopted to determine the amount of hydrogen production on an 80/100 PORAPAK N molecule column. The temperature of the thermal conductivity detector, column box, and filament was assigned at 200,  $150^\circ\text{C}$ , and  $300^\circ\text{C}$ , respectively, and the gas flow rate is  $10 \text{ mL}/\text{min}$  in the constant pressure mode. The holding pressure is  $60.0 \text{ kPa}$  and the ion mode is in negative ion mode. After preheating the gas chromatography,  $300 \mu\text{L}$  of air for zero adjustments was injected. After each irradiation for one hour,  $300 \mu\text{L}$  of gas was taken out to analyze the quantity of hydrogen according to the peak areas with the retention time around  $0.625\text{--}0.630 \text{ min}$  through the external standard method.

### 3. Results and Discussion

**3.1. XRD Analysis.** XRD was employed to investigate the crystal phase structures of the samples as shown in Figure 1, and the characteristic peaks of pure  $\text{TiO}_2$  corresponding to both anatase and rutile were observed. The peaks at  $2\theta$  of  $25.3^\circ$ ,  $37.9^\circ$ ,  $48.2^\circ$ , and  $62.7^\circ$  were indexed to (101), (004), (200), and (204) planes of anatase  $\text{TiO}_2$  (PDF NO. 21-1272), and those at  $2\theta$  of  $27.4^\circ$ ,  $36.1^\circ$ ,  $41.2^\circ$ , and  $54.3^\circ$  corresponded to (110), (101), (111), and (211) planes of rutile  $\text{TiO}_2$  (PDF NO. 21-1276), respectively [33]. For  $\text{WO}_3/\text{TiO}_2$  nanofibers, the diffraction peaks of were similar to those of  $\text{TiO}_2$  nanofibers and the peak intensities gradually decreased with the increase of  $\text{WO}_3$  content and characteristic peaks corresponding to rutile phase diminished in 10%  $\text{WO}_3/\text{TiO}_2$  samples, indicating that the introduction of  $\text{WO}_3$  into  $\text{TiO}_2$  affected the crystal structure of  $\text{TiO}_2$ . In addition, no diffraction peaks related to  $\text{WO}_3$  were detected which might be due to its high dispersion or low content [34].

**3.2. Photocatalytic Degradation Performance.** The photocatalytic performance of  $\text{TiO}_2$  and  $\text{WO}_3/\text{TiO}_2$  nanofibers was assessed by degrading MB under Xenon lamp illumination. The experimental results are displayed in Figure 2(a). Apparently, as shown in Figure 2(a), 5%  $\text{WO}_3/\text{TiO}_2$  exhibited the highest photocatalytic activity with the elimination rate of 96.2% for MB within 150 min, in comparison with that of  $\text{TiO}_2$  nanofibers (72.0%), 1%  $\text{WO}_3/\text{TiO}_2$  (91.5%) nanofibers, and 10%  $\text{WO}_3/\text{TiO}_2$  nanofibers (79.0%) under the same condition. This result indicates that the content of  $\text{WO}_3$  in  $\text{WO}_3/\text{TiO}_2$  composites had a significant effect on the degradation efficiency of MB. The reasons could be attributed to

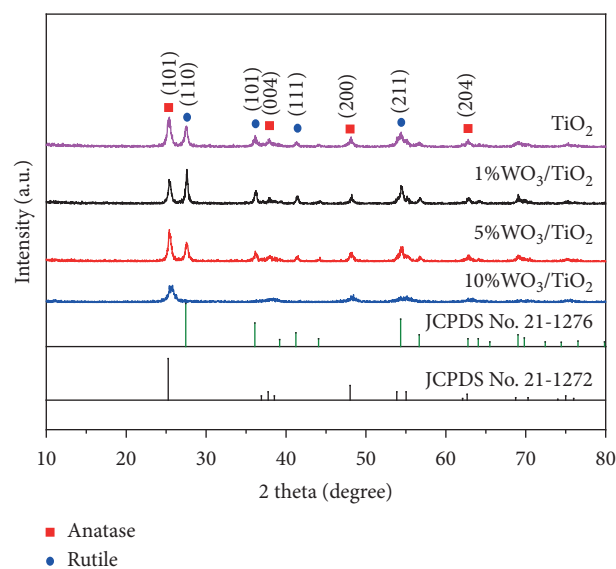


FIGURE 1: XRD patterns of  $\text{TiO}_2$  and  $\text{WO}_3/\text{TiO}_2$  nanofibers.

the following: the lower the amount of  $\text{WO}_3$  is, the less the electron transfer center can be formed, leading to the low photocatalytic activity; on the contrary, too much amount of  $\text{WO}_3$  might change the electron transfer centers to the electron-hole recombination centers; in addition, the  $\text{W}^{6+}$  could scramble electrons from  $\text{TiO}_2$ ; all of these lead to the low photocatalytic activity. In terms of the charge layer thickness, excessive doping of  $\text{WO}_3$  can make the depth of incident light less than the surface charge layer thickness, decreased potential difference, and reduced the electron-hole migration force. Thus, the recombination of photogenerated electrons and holes becomes more easily. Moreover, the larger specific surface area of 5%  $\text{WO}_3/\text{TiO}_2$  nanofibers could supply more magnificent active sites, resulting in the promoted photocatalytic performance.

The photocatalytic activity of 5%  $\text{WO}_3/\text{TiO}_2$  nanofibers is shown in Figure 2(b). With the photocatalytic degradation, the absorption peak at  $664 \text{ nm}$  blueshifts and turns broadened at the same time, which may be caused by the gradual deethylation of MB [35]. The strong chromophore and conjugated structure of MB were destroyed during degradation [36]. Those characteristic peaks disappeared after 150 min irradiation, indicating that the aromatic rings and the conjugated  $\pi$  bond in the MB molecules were completely broken [34]. Obviously, 5%  $\text{WO}_3/\text{TiO}_2$  nanofibers could degrade MB completely under illumination.

The significant stability of the photocatalyst was very substantial for its practical applications. To confirm the stability of 5%  $\text{WO}_3/\text{TiO}_2$  nanofibers, recycling degradation tests were conducted by successive batches degradation of MB as shown in Figure 3. It was clear that at the end of the 5<sup>th</sup> cycle, 5%  $\text{WO}_3/\text{TiO}_2$  nanofibers could still degrade 93% MB within 140 min (shown in Figure 3(a)) under Xenon lamp illumination, indicating the high stability of 5%  $\text{WO}_3/\text{TiO}_2$  nanofibers. The crystal structure of used 5%  $\text{WO}_3/\text{TiO}_2$  nanofibers was also determined to be stable as shown in Figure 3(b). In summary, 5%  $\text{WO}_3/\text{TiO}_2$  nanofibers showed

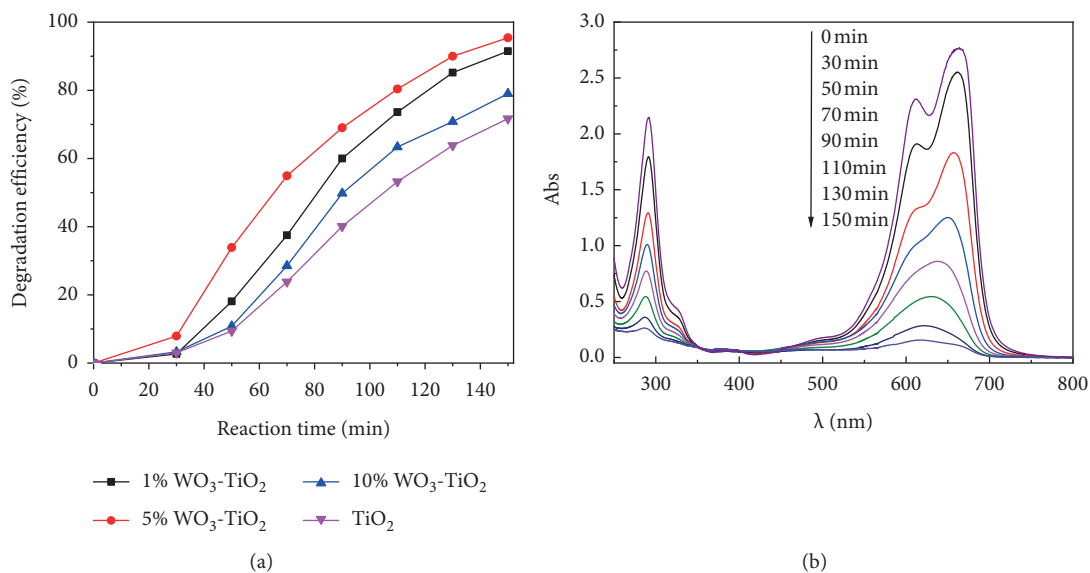


FIGURE 2: (a) Decomposition of MB by TiO<sub>2</sub> and WO<sub>3</sub>/TiO<sub>2</sub> nanofibers; (b) UV-Vis absorption spectra of MB during the photodegradation process by 5% WO<sub>3</sub>/TiO<sub>2</sub> nanofibers.

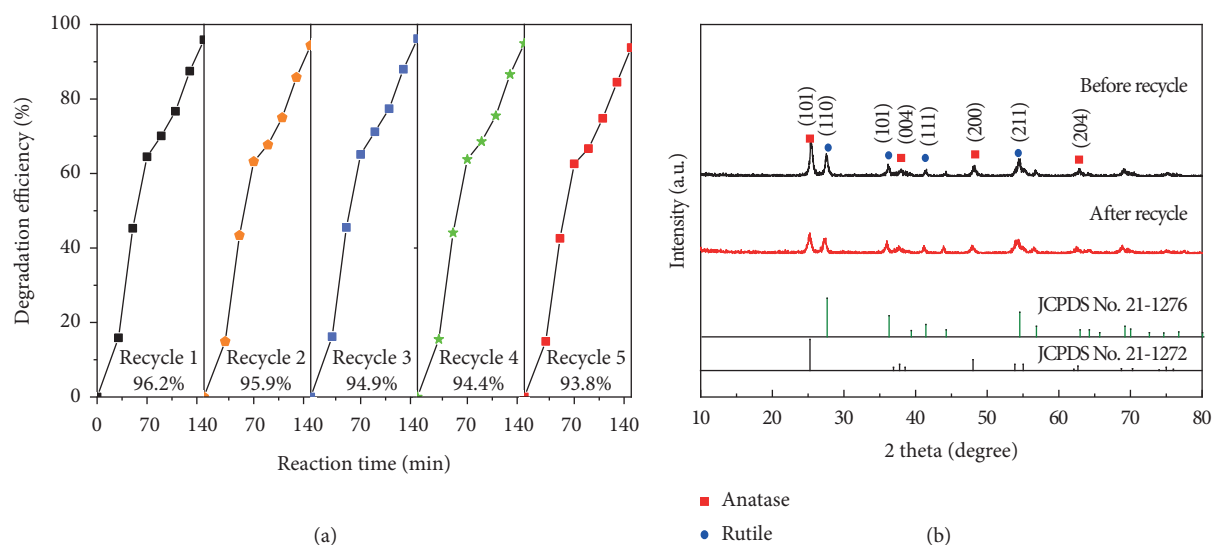


FIGURE 3: (a) Photodegradation performance within five cycles for 5% WO<sub>3</sub>/TiO<sub>2</sub> nanofibers; (b) XRD patterns of 5% WO<sub>3</sub>/TiO<sub>2</sub> nanofibers before and after photocatalysis.

high photocatalytic activity and stability in the catalytic process.

**3.3. Photocurrent Analysis.** The photocurrent test is one of the important means to characterize the response intensity of carriers to illumination and the difficulty of carrier separation. A common method for detecting photocurrent is to use a photocatalyst as a working electrode and a saturated calomel electrode as a reference electrode. When light is irradiated, due to the photoelectric effect, the movement of

the electrons emitted by the electrode will form a photocurrent. The intensity of the generated photocurrent is closely related to the nature of the photocatalyst, and the intensity of the photocurrent is directly proportional to the separation efficiency of photogenerated carriers.

The TiO<sub>2</sub> and WO<sub>3</sub>/TiO<sub>2</sub> nanofibers were coated on the glass plate as the working electrode (coating amount is 3 mg), and the working electrode was irradiated by the 125 W Mercury lamp every 10 s, and the cycle was repeated. The results are shown in Figure 4. It can be seen from Figure 4 that the photocurrent response intensity of WO<sub>3</sub>/

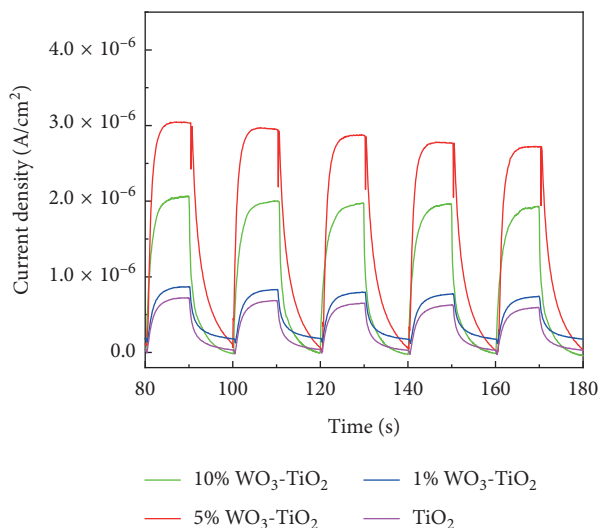


FIGURE 4: Photocurrent response curves of  $\text{TiO}_2$  and  $\text{WO}_3/\text{TiO}_2$  nanofibers.

$\text{TiO}_2$  nanofibers is higher than that of  $\text{TiO}_2$  nanofibers ( $0.7 \times 10^{-6} \text{ A/cm}^2$ ), which indicates that the doping of  $\text{WO}_3$  improves the separation efficiency of photogenerated carriers. 5%  $\text{WO}_3/\text{TiO}_2$  nanofibers have the highest photocurrent response intensity, reaching  $3.0 \times 10^{-6} \text{ A/cm}^2$ , indicating that the light-induced electron-hole pairs are effectively separated in the 5%  $\text{WO}_3/\text{TiO}_2$  nanofiber system, and the recombination trend is lower.

Based on the above analysis results, we believe that 5%  $\text{WO}_3/\text{TiO}_2$  nanofibers are the best composite percentage samples, and their comprehensive performance is the best. Therefore, 5%  $\text{WO}_3/\text{TiO}_2$  nanofibers were further characterized and their hydrogen production performance was studied.

**3.4. SEM and EDS Analysis.** The SEM images of  $\text{TiO}_2$  and 5%  $\text{WO}_3/\text{TiO}_2$  nanofibers are displayed in Figure 5. From Figures 5(a) and 5(c), it was clear that the  $\text{TiO}_2$  precursor and 5%  $\text{WO}_3/\text{TiO}_2$  precursor were composed of smooth fibers with about 200 nm in diameter and 20–30  $\mu\text{m}$  in length. After calcination, these smooth fibers fractured to short fibers with several hundred nanometers in length and the surface became rough as shown in Figures 5(b) and 5(d), which might be resulting from the oxidative decomposition of precursor fibers. As we all know, a rough surface possessed a larger surface area and is conducive to the adsorption reaction, which is helpful to improve the photocatalytic activity [37].

To further identify the chemical composition of both  $\text{TiO}_2$  nanofibers and 5%  $\text{WO}_3/\text{TiO}_2$  nanofibers, EDS analysis was conducted, and the results are illustrated in Figure 6. As expected,  $\text{TiO}_2$  nanofibers were composed of Ti, O elements as shown in Figure 6(a). Three Ti, O, and W elements were detected in 5%  $\text{WO}_3/\text{TiO}_2$  nanofibers as shown in Figure 6(b), implying the successful incorporation of  $\text{WO}_3$  into  $\text{TiO}_2$  nanofibers. Table 1 shows the element contents of

$\text{TiO}_2$  and 5%  $\text{WO}_3/\text{TiO}_2$  samples, which were basically consistent with the raw material ratio in the precursor.

**3.5. XPS Analysis.** The surface chemical status and elemental composition of the as-prepared 5%  $\text{WO}_3/\text{TiO}_2$  nanofibers were analyzed by XPS. Figure 7(a) demonstrates the survey XPS spectra of sample, which indicated that 5%  $\text{WO}_3/\text{TiO}_2$  nanofibers consisted of Ti, W, and O elements, in consistent with EDS results (Figure 6(b)). As indicated in Figure 7(b), the typical peak at 285.49 eV could be ascribed to the carbon contamination in the XPS measurements [38] or organic residues from raw material PVP while calcination [23]. Figure 7(c) displays the high-resolution XPS spectra of O1s with the binding energy at 530.69 eV, which could be attributed to O atom in Ti-O bond and W-O; they share the orbital O1s [26, 39]. The binding energies of Ti  $2p_{3/2}$  and Ti  $2p_{1/2}$  at 459.3 and 464.8 eV in Figure 7(d) confirmed the existence of  $\text{Ti}^{4+}$  in 5%  $\text{WO}_3/\text{TiO}_2$  [40]. The peaks centered at 37.52 and 35.78 eV in Figure 7(e) were attributed to W  $4f_{5/2}$  and W  $4f_{7/2}$ , which fitted well with the characteristic peaks of  $\text{W}^{6+}$  [30].

**3.6. UV-Vis DRS Analysis.** The optical absorption property of  $\text{TiO}_2$  and 5%  $\text{WO}_3/\text{TiO}_2$  nanofibers was characterized by UV-Vis diffuse reflectance technique. Figure 8(a) indicated that the light absorption ability of 5%  $\text{WO}_3/\text{TiO}_2$  nanofibers was slightly enhanced compared with  $\text{TiO}_2$  nanofibers. The band gaps of  $\text{TiO}_2$  and 5%  $\text{WO}_3/\text{TiO}_2$  nanofibers were evaluated according to the equation [41]  $(\alpha h\nu)^2 = A(h\nu - E_g)$ , where  $A$  is a constant,  $h$  is Planck's constant,  $\nu$  is the photon frequency,  $\alpha$  is the absorption coefficient (replaced with absorbance in the calculation), and  $E_g$  is the band gap energy. Figure 8(b) displays the plots of  $(\alpha h\nu)^2$  versus  $(h\nu)$  and the band gap energy of  $\text{TiO}_2$  and 5%  $\text{WO}_3/\text{TiO}_2$  nanofibers was estimated to be 3.23 eV and 3.16 eV, respectively, by extrapolating the linear portion of the graphs to energy axis.

**3.7. BET Analysis.**  $\text{N}_2$  adsorption-desorption measurements were conducted to characterize the specific surface areas and pore size distributions of  $\text{TiO}_2$  and 5%  $\text{WO}_3/\text{TiO}_2$  nanofibers. According to the International Union of Pure and Applied Chemistry (IUPAC) classification, the  $\text{N}_2$  adsorption-desorption isotherms of both  $\text{TiO}_2$  and 5%  $\text{WO}_3/\text{TiO}_2$  nanofibers in Figure 9(a) all corresponded to type IV with the obvious H3-type hysteresis loops, indicating the existence of large mesopores. Figure 9(b) shows the Barret-Joyner-Halenda (BJH) pore size distribution curves of  $\text{TiO}_2$  and 5%  $\text{WO}_3/\text{TiO}_2$  nanofibers. The pore size of  $\text{TiO}_2$  and 5%  $\text{WO}_3/\text{TiO}_2$  nanofibers was mainly distributed in the range of 2–10 nm, further confirming the existence of mesopores. In addition, the BET specific surface areas and detailed BJH pore size of  $\text{TiO}_2$  and 5%  $\text{WO}_3/\text{TiO}_2$  nanofibers are listed in Table 2. The 5%  $\text{WO}_3/\text{TiO}_2$  nanofibers had a larger surface area ( $51.457 \text{ m}^2/\text{g}$ ) than that of  $\text{TiO}_2$  ( $45.067 \text{ m}^2/\text{g}$ ), implying that the coupling of  $\text{WO}_3$  with  $\text{TiO}_2$  boosts the specific surface areas and provided abundant active sites for

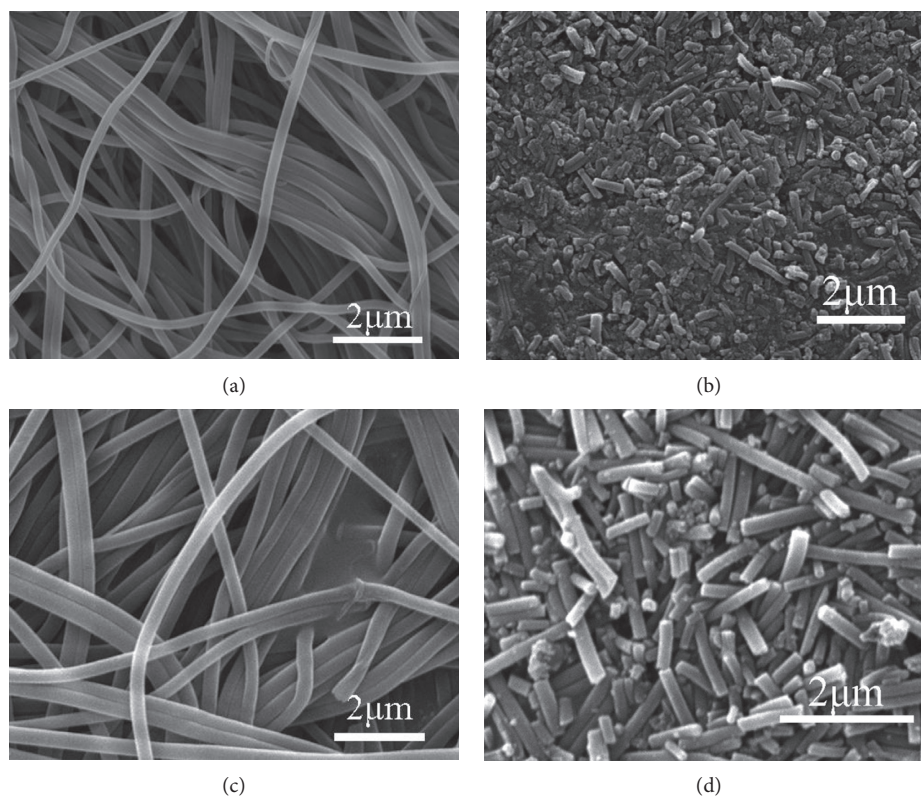


FIGURE 5: SEM patterns of  $\text{TiO}_2$  precursor (a),  $\text{TiO}_2$  nanofibers (b), 5%  $\text{WO}_3/\text{TiO}_2$  precursor (c), and 5%  $\text{WO}_3/\text{TiO}_2$  nanofibers (d).

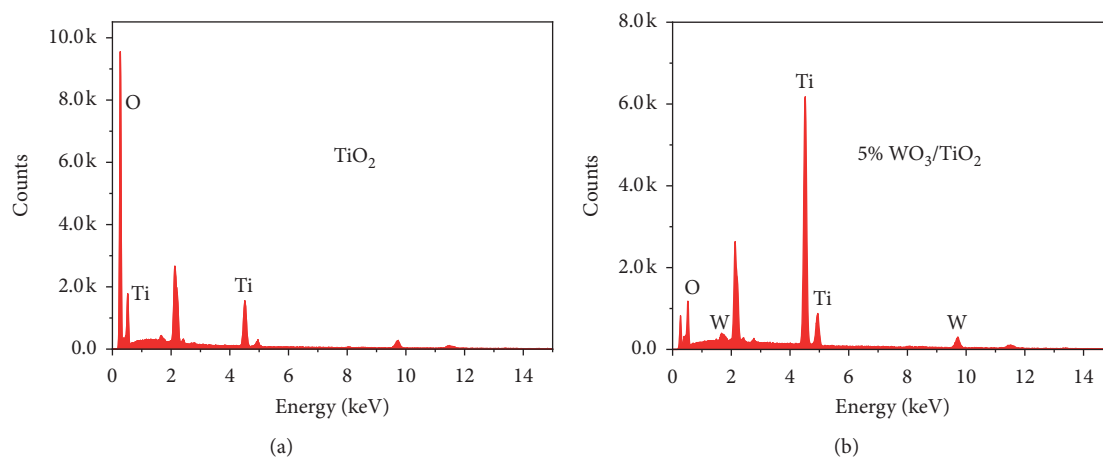


FIGURE 6: EDS of  $\text{TiO}_2$  (a) and 5%  $\text{WO}_3/\text{TiO}_2$  (b) nanofibers.

TABLE 1: Elemental composition and content of  $\text{TiO}_2$  and 5%  $\text{WO}_3/\text{TiO}_2$  nanofibers.

Sample	Element	Weight percentage	Atomic percentage
$\text{TiO}_2$	O	39.89	66.02
	Ti	60.11	32.89
5% $\text{WO}_3/\text{TiO}_2$	O	37.21	67.18
	Ti	51.87	31.17
	W	10.52	1.64

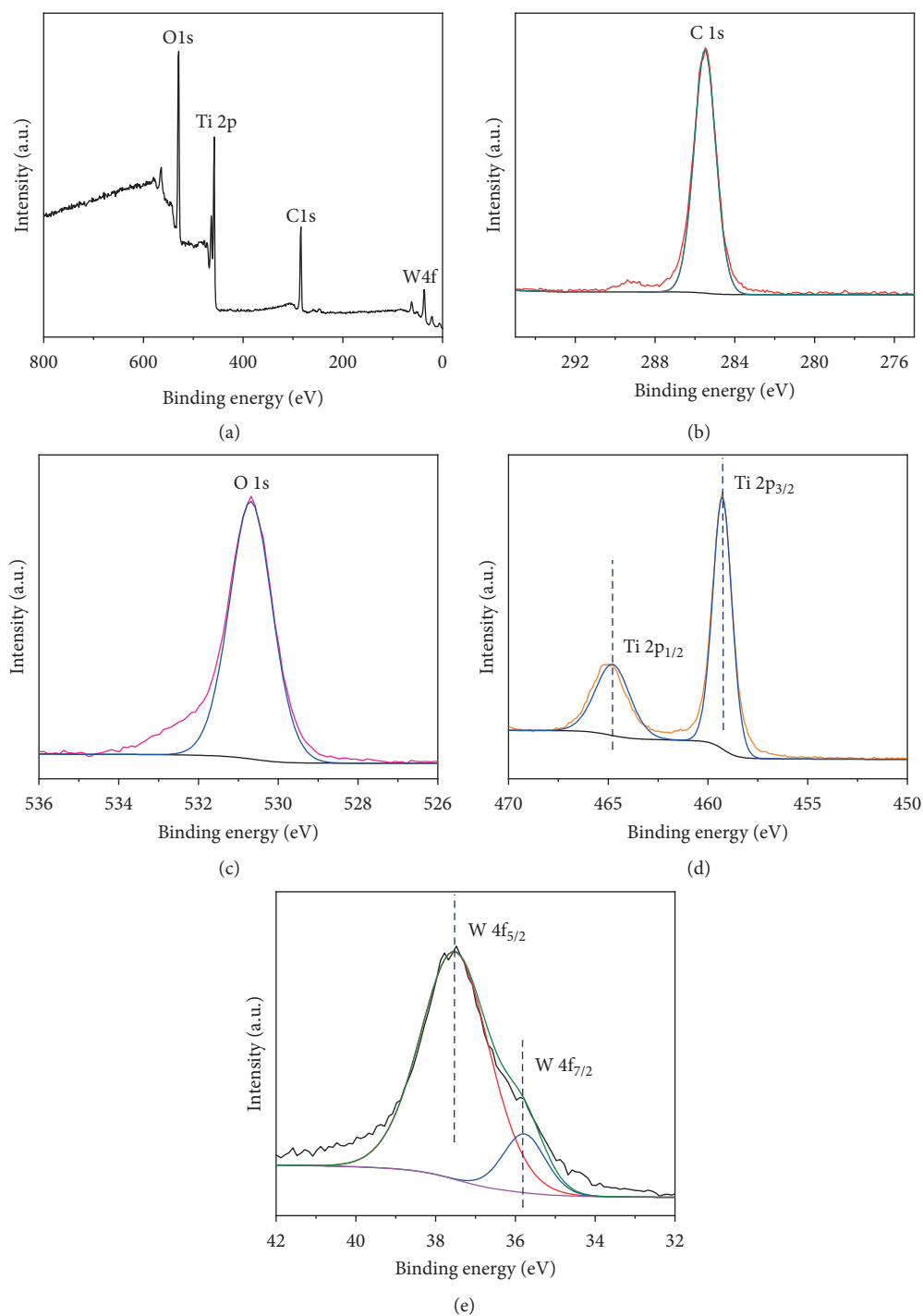


FIGURE 7: XPS spectra of 5%  $\text{WO}_3/\text{TiO}_2$  nanofibers. (a) Survey spectra, (b) C 1s, (c) O 1s, (d) Ti 2p, and (e) W 4f.

adsorption and surface reactions, which could be attributed to their rough surface as shown in Figure 5(d).

**3.8. Photocatalytic Hydrogen Production Performance.** Hydrogen production performance of 5%  $\text{WO}_3/\text{TiO}_2$  nanofibers by water splitting was evaluated under 100 W Mercury lamp irradiation. The  $\text{Na}_2\text{S}$  solution and  $\text{Na}_2\text{SO}_3$  solution were added to splitting water to capture

photogenerated holes and accelerate the outward migration of photogenerated electrons, which is conducive to  $\text{H}_2$  generation. Figure 10(a) shows the photocatalytic  $\text{H}_2$  evolution capabilities of  $\text{WO}_3$ ,  $\text{TiO}_2$ , and 5%  $\text{WO}_3/\text{TiO}_2$  nanofibers. It was obvious that  $\text{WO}_3$  exhibits no  $\text{H}_2$  generation activity, perhaps due to the higher positive CB potential (0.79 eV) [42] than  $\text{H}^+/\text{H}_2\text{O}$  (-0.33 eV), while  $\text{TiO}_2$  nanofibers display a relatively low photocatalytic  $\text{H}_2$  production activity with  $73.32 \mu\text{mol}\cdot\text{g}^{-1}\cdot\text{h}^{-1}$ , due to the rapid

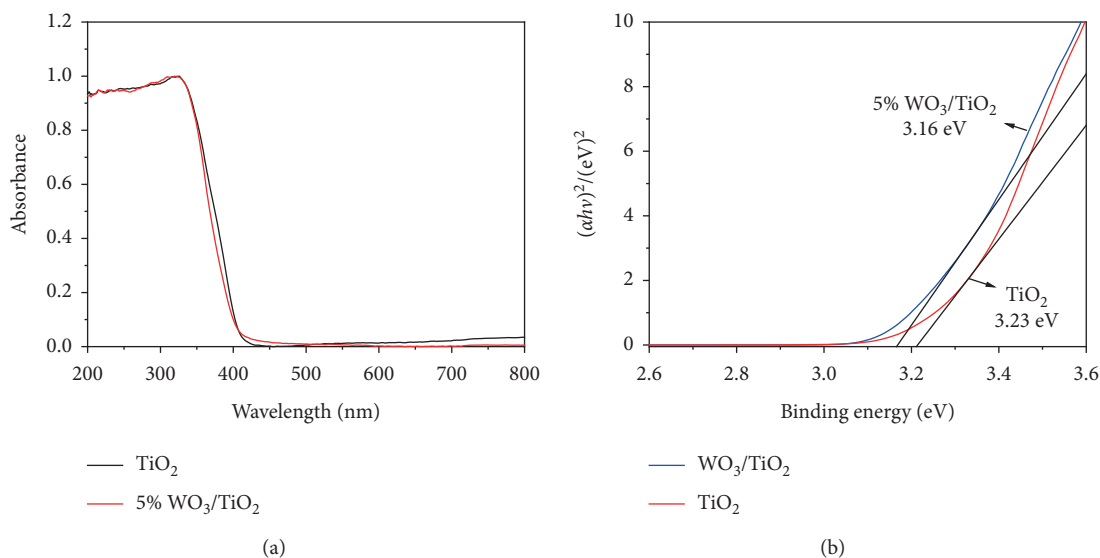


FIGURE 8: UV-Vis DRS spectra of  $\text{TiO}_2$  and 5%  $\text{WO}_3/\text{TiO}_2$  nanofibers.

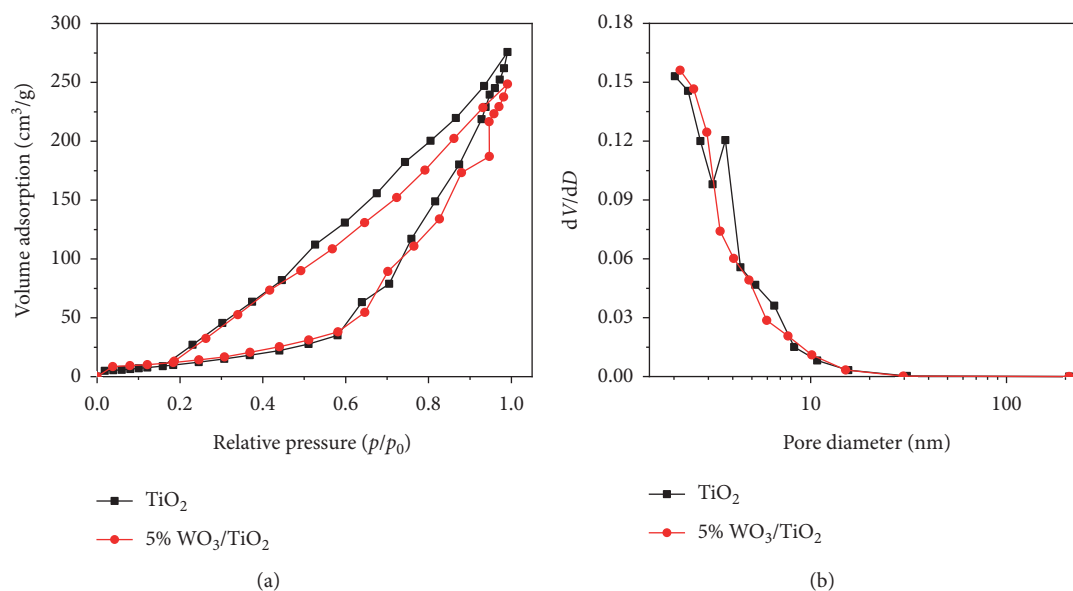


FIGURE 9:  $\text{N}_2$  adsorption and desorption isotherms (a) and the BJH pore size distribution of  $\text{TiO}_2$  and 5%  $\text{WO}_3/\text{TiO}_2$  nanofibers (b).

TABLE 2: Specific surface area, average pore size, and pore volume of  $\text{TiO}_2$  and 5%  $\text{WO}_3/\text{TiO}_2$  nanofibers.

Sample	$S_{\text{BET}}$ ( $\text{m}^2/\text{g}$ )	APS (nm)	PV ( $\text{cm}^3/\text{g}$ )
$\text{TiO}_2$	45.067	4.678	0.635
5% $\text{WO}_3/\text{TiO}_2$	51.457	4.737	0.563

$S_{\text{BET}}$ : specific surface area; APS: average pore size; PV: pore volume.

recombination of electrons in CB and holes in VB. For the 5%  $\text{WO}_3/\text{TiO}_2$  nanofibers, the  $\text{H}_2$  yield rate was  $107.15 \mu\text{mol}\cdot\text{g}^{-1}\cdot\text{h}^{-1}$  which was approximately 1.5 times that of  $\text{TiO}_2$  nanofibers. This result can be attributed to the formation of  $\text{WO}_3/\text{TiO}_2$  Z-scheme heterostructure, which can effectively separate useful electrons and holes, and the

relatively useless electrons and holes are compounded nearby. In other words, the photoinduced electrons were injected onto the CB of  $\text{TiO}_2$ , while the holes were migrated onto the VB of  $\text{WO}_3$ . Thus the recombination of photo-generated charge carriers was effectively inhibited. As a result, the reduction of  $\text{H}^+$  to  $\text{H}_2$  could easily be achieved on 5%

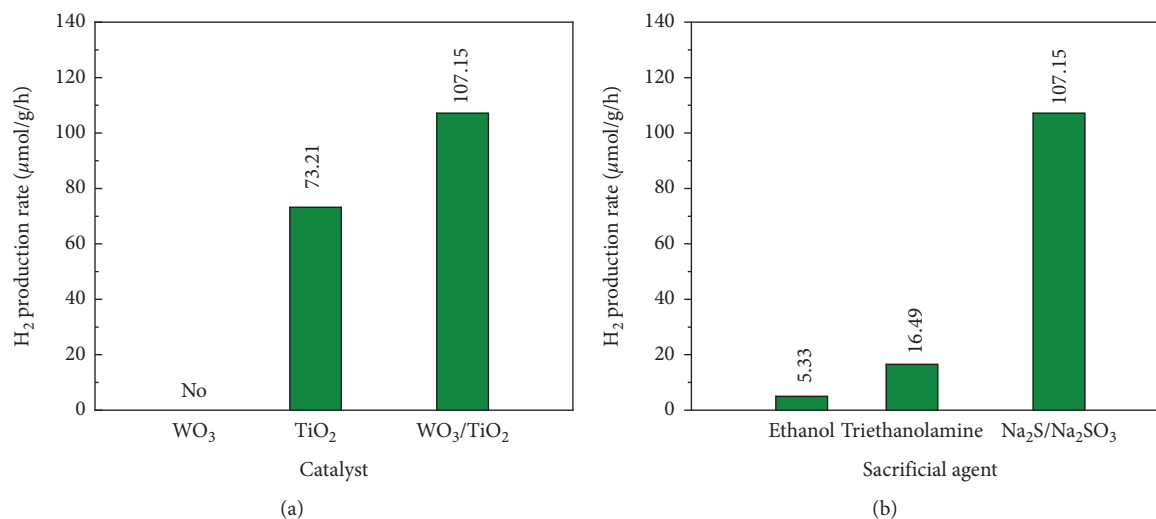


FIGURE 10: (a) H<sub>2</sub> production rate over WO<sub>3</sub>, TiO<sub>2</sub>, and 5% WO<sub>3</sub>/TiO<sub>2</sub> nanofibers. (b) H<sub>2</sub> production rate from different sacrificial agents over 5% WO<sub>3</sub>/TiO<sub>2</sub> nanofibers.

WO<sub>3</sub>/TiO<sub>2</sub> nanofibers system by electrons, while the holes were reacted with S<sup>2-</sup> and SO<sub>3</sub><sup>2-</sup>.

Some photocatalytic materials can only oxidize (electron acceptor) or reduce (electron donor) water to generate oxygen or hydrogen with the participation of sacrificial agents (including electron acceptor and electron donor). Therefore, sacrificial agents are widely used to verify the photocatalytic properties of the materials. The selection of the sacrificial agent has a great influence on hydrogen production. In this experiment, Na<sub>2</sub>S/Na<sub>2</sub>SO<sub>3</sub>, triethanolamine, and ethanol were selected as electron donors, which are combined with photogenerated holes to promote hydrogen production and prevent photocorrosion. From Figure 10(b), it was apparent that the mixture of Na<sub>2</sub>S/Na<sub>2</sub>SO<sub>3</sub> was the best sacrificial agents for hydrogen evolution over 5% WO<sub>3</sub>/TiO<sub>2</sub> photocatalyst.

Therefore, the reason why 5% WO<sub>3</sub>/TiO<sub>2</sub> nanofibers have high hydrogen production activity may be that, on the one hand, the structure of the catalyst is Z-scheme heterojunction, which reduces the recombination probability of photogenerated electrons and holes; on the other hand, the addition of Na<sub>2</sub>S and Na<sub>2</sub>SO<sub>3</sub> hole trapping agents further inhibits the recombination of photogenerated electrons and holes.

**3.9. Photocatalytic Mechanism Analysis.** The band edge positions of 5% WO<sub>3</sub>/TiO<sub>2</sub> nanofibers were theoretically calculated by the following empirical equation [43]:

$$\begin{aligned} E_{\text{CB}} &= E_{\text{VB}} - E_g, \\ E_{\text{VB}} &= X - E_e + 0.5E_g, \end{aligned} \quad (1)$$

where  $X$  is the electronegativity of the semiconductor ( $X_{\text{TiO}_2} = 5.81$  eV and  $X_{\text{WO}_3} = 6.59$  eV [44]),  $E_e$  is the energy of free electrons on the hydrogen scale ( $\approx 4.5$  eV), and  $E_g$  is the band gap energy of the semiconductor ( $E_{g\text{TiO}_2} = 3.23$  eV and

$E_{g\text{WO}_3} = 2.6$  eV). According to this empirical expression, the calculated CB ( $E_{\text{CB}}$ ) and VB ( $E_{\text{VB}}$ ) edge positions for WO<sub>3</sub> and TiO<sub>2</sub> are displayed in Figure 11(a). The CB potential of WO<sub>3</sub> (+0.79 eV) is more negative than the VB of TiO<sub>2</sub> (-0.31 eV) but more positive than the CB of TiO<sub>2</sub> (+2.93 eV); therefore, a Z-scheme charges transportation system is formed between WO<sub>3</sub> and TiO<sub>2</sub>. The photoinduced electrons on the CB of TiO<sub>2</sub> can efficiently inject onto the CB of WO<sub>3</sub> and the holes on VB of WO<sub>3</sub> can transfer onto the VB of TiO<sub>2</sub>. As a result, the highly effective separation and migration system are generated for boosting the photocatalytic performance of 5% WO<sub>3</sub>/TiO<sub>2</sub> composite nanofibers.

To further elucidate the photocatalytic mechanism and identify the main reactive species in the MB degradation process, the active species trapping experiment was conducted. The detailed free radical capture experiment processes were similar to the photocatalytic activity experiments. The reactive free species in MB photocatalytic process over 5% WO<sub>3</sub>/TiO<sub>2</sub> nanofibers were identified by using isopropanol (IPA), benzoquinone (BQ), sodium ethylenediaminetetraacetic acid (Na<sub>2</sub>EDTA), and potassium bromate (KBrO<sub>3</sub>) as scavengers of ·OH, ·O<sub>2</sub><sup>-</sup>, h<sup>+</sup>, and e<sup>-</sup>, respectively. As indicated in Figure 11(b), with the addition of IPA, BQ, and Na<sub>2</sub>EDTA, the degradation efficiency of MB declined to 60.3%, 42.3%, and 60.5%, indicating that H<sub>2</sub>O and/or OH<sup>-</sup> trap h<sup>+</sup> and turn into ·OH in the system. The addition of BQ did not show a significant impact on the photocatalytic activity, indicating that no ·O<sub>2</sub><sup>-</sup> radicals involved in the process. The comparison results confirmed that ·OH, h<sup>+</sup>, and e<sup>-</sup> are the dominant reactive radicals in the MB photodegradation process. ·OH with strong oxidation ability (the standard redox potential is +2.8 eV) can oxidize most organic dyes. Due to the formation of Z-scheme heterojunction, the photogenerated electrons and holes were transferred onto the CB of TiO<sub>2</sub> and VB of WO<sub>3</sub>, respectively. As the CB level of TiO<sub>2</sub> (-0.31 eV) is close to the potential value of ·O<sub>2</sub><sup>-</sup>/O<sub>2</sub> (-0.33 eV) [45], ·O<sub>2</sub><sup>-</sup> could not be

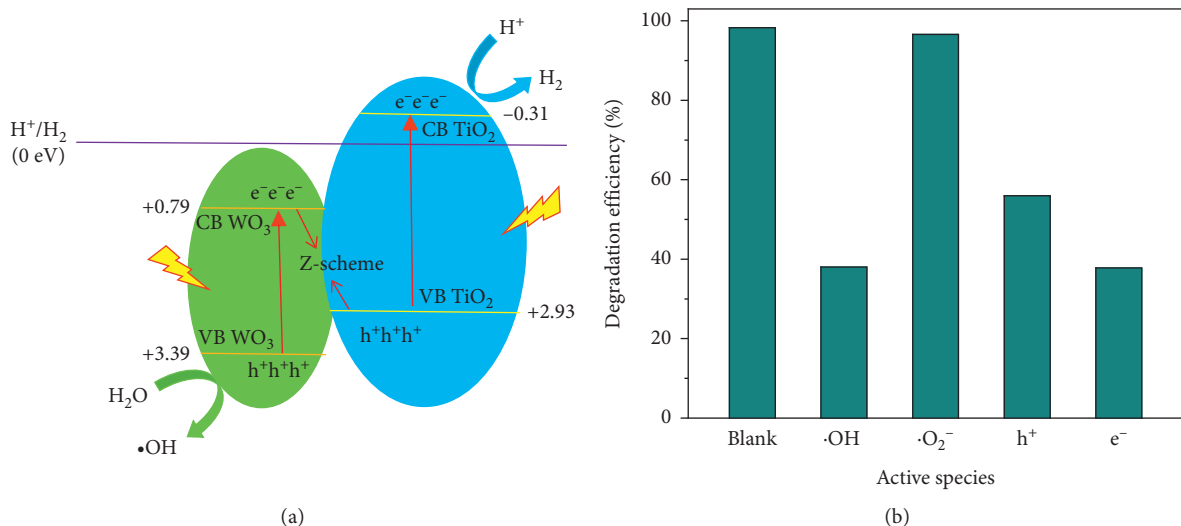


FIGURE 11: (a) Z-scheme charge transfer and surface redox reactions for 5% WO<sub>3</sub>/TiO<sub>2</sub> nanofibers. (b) Catalytic degradation of MB over 5% WO<sub>3</sub>/TiO<sub>2</sub> nanofibers with different quenchers.

formed on TiO<sub>2</sub>. Since holes are accumulated on VB of WO<sub>3</sub> with more positive potential (+3.39 eV) than the redox potential of ·OH/OH<sup>-</sup> (+2.27 eV) [45], therefore, large amounts of ·OH are generated in 5% WO<sub>3</sub>/TiO<sub>2</sub> composite nanofibers.

The highest photocurrent response intensity of 5% WO<sub>3</sub>/TiO<sub>2</sub> nanofibers further confirmed that intimate contact between TiO<sub>2</sub> and WO<sub>3</sub> could efficiently separate the photogenerated charge carriers and accelerate efficient charge transfer [34, 46].

#### 4. Conclusions

In this paper, highly efficient WO<sub>3</sub>/TiO<sub>2</sub> nanofibers were prepared by the electrospinning method. The mole percentage of W and Ti in the composite fibers has an important influence on their performance. The optimized 5% WO<sub>3</sub>/TiO<sub>2</sub> nanofibers exhibited tremendous enhanced photocatalytic degradation capability for MB solution with a 96.2% removal rate under the Xenon lamp irradiation. In addition, under the irradiation of Mercury lamp, the photocatalytic H<sub>2</sub> production rate over 5% WO<sub>3</sub>/TiO<sub>2</sub> nanofibers is 107.15 μmol·g<sup>-1</sup>·h<sup>-1</sup>, which is about 1.5 times of TiO<sub>2</sub> nanofibers. The enhanced activity may be due to the formation of Z-scheme heterojunction, which is conducive to the effective separation and transfer of photoinduced carriers. It could be seen from the experimental results of free radical trapping that ·OH was the main oxidant for MB degradation. Our work provides a useful reference for the preparation of other TiO<sub>2</sub> based photocatalysts towards both solar energy conversion and wastewater recovery.

#### Data Availability

All the data generated or analyzed during this study are included within the article.

#### Conflicts of Interest

The authors declare that there are no conflicts of interest regarding the publication of this paper.

#### Acknowledgments

This work was supported by the National Natural Science Foundation of China (21767008), Research initiation fund of Hainan University (KYQD(ZR)1993), and Hainan Natural Science Foundation (218QN187).

#### References

- [1] T. Jiao, H. Zhao, J. Zhou et al., "Self-assembly reduced graphene oxide nanosheet hydrogel fabrication by anchorage of chitosan/silver and its potential efficient application toward dye degradation for wastewater treatments," *ACS Sustainable Chemistry & Engineering*, vol. 3, no. 12, pp. 3130–3139, 2015.
- [2] L. Ge, M. Zhang, R. Wang et al., "Fabrication of CS/GA/RGO/Pd composite hydrogels for highly efficient catalytic reduction of organic pollutants," *RSC Advances*, vol. 10, no. 26, pp. 15091–15097, 2020.
- [3] Y. Feng, J. Yin, S. Liu, Y. Wang, B. Li, and T. Jiao, "Facile synthesis of Ag/Pd nanoparticle-loaded poly(ethylene imine) composite hydrogels with highly efficient catalytic reduction of 4-nitrophenol," *ACS Omega*, vol. 5, no. 7, pp. 3725–3733, 2020.
- [4] A. Fujishima and K. Honda, "Electrochemical photolysis of water at a semiconductor electrode," *Nature*, vol. 238, no. 5358, pp. 37–38, 1972.
- [5] Z. Xing, J. Zhang, J. Cui et al., "Recent advances in floating TiO<sub>2</sub>-based photocatalysts for environmental application," *Applied Catalysis B: Environmental*, vol. 225, pp. 452–467, 2018.
- [6] L. Wu, S. Shi, Q. Li, X. Zhang, and X. Cui, "TiO<sub>2</sub> nanoparticles modified with 2D MoSe<sub>2</sub> for enhanced photocatalytic activity on hydrogen evolution," *International Journal of Hydrogen Energy*, vol. 44, no. 2, pp. 720–728, 2019.

- [7] A. Hajjaji, S. Jemai, A. Rebhi et al., "Enhancement of photocatalytic and photoelectrochemical properties of TiO<sub>2</sub> nanotubes sensitized by SILAR-deposited PbS nanoparticles," *Journal of Materiomics*, vol. 6, no. 1, pp. 62–69, 2020.
- [8] J. Liu, S. Zou, L. Lu, H. Zhao, L. Xiao, and J. Fan, "Room temperature selective oxidation of benzyl alcohol under base-free aqueous conditions on Pt/TiO<sub>2</sub>," *Catalysis Communications*, vol. 99, pp. 6–9, 2017.
- [9] A. J. Jafari, M. Kermani, A. Hosseini-Bandegharai et al., "Synthesis and characterization of Ag/TiO<sub>2</sub>/composite aerogel for enhanced adsorption and photo-catalytic degradation of toluene from the gas phase," *Chemical Engineering Research and Design*, vol. 150, pp. 1–13, 2019.
- [10] S. Suphankij, W. Mekprasart, and W. Pecharapa, "Photocatalytic of N-doped TiO<sub>2</sub> nanofibers prepared by electrospinning," *Energy Procedia*, vol. 34, pp. 751–756, 2013.
- [11] C. O. Amor, K. Kais elghniji, C. Virlan, A. Pui, and E. Elaloui, "Effect of dysprosium ion (Dy<sub>3+</sub>) doping on morphological, crystal growth and optical properties of TiO<sub>2</sub> particles and thin films," *Physica B: Condensed Matter*, vol. 560, pp. 67–74, 2019.
- [12] Y. Xu, R. Ahmed, D. Klein et al., "Improving photo-oxidation activity of water by introducing Ti<sub>3+</sub> in self-ordered TiO<sub>2</sub> nanotube arrays treated with Ar/NH<sub>3</sub>," *Journal of Power Sources*, vol. 414, pp. 242–249, 2019.
- [13] D. Sánchez-Rodríguez, M. G. Méndez Medrano, H. Remita, and V. Escobar-Barrios, "Photocatalytic properties of BiOCl-TiO<sub>2</sub> composites for phenol photodegradation," *Journal of Environmental Chemical Engineering*, vol. 6, no. 2, pp. 1601–1612, 2018.
- [14] K. Li, T. Jiao, R. Xing et al., "Fabrication of tunable hierarchical MXene@AuNPs nanocomposites constructed by self-reduction reactions with enhanced catalytic performances," *Science China Materials*, vol. 61, no. 5, pp. 728–736, 2018.
- [15] X. Xing, H. Zhu, M. Zhang, L. Xiao, Q. Li, and J. Yang, "Effect of heterojunctions and phase-junctions on visible-light photocatalytic hydrogen evolution in BCN-TiO<sub>2</sub> photocatalysts," *Chemical Physics Letters*, vol. 727, pp. 11–18, 2019.
- [16] Y. Li, P. Zhang, D. Wan, C. Xue, J. Zhao, and G. Shao, "Direct evidence of 2D/1D heterojunction enhancement on photocatalytic activity through assembling MoS<sub>2</sub> nanosheets onto super-long TiO<sub>2</sub> nanofibers," *Applied Surface Science*, vol. 504, pp. 144361–144370, 2020.
- [17] C. Chen, J. Zhou, J. Geng et al., "Perovskite LaNiO<sub>3</sub>/TiO<sub>2</sub> step-scheme heterojunction with enhanced photocatalytic activity," *Applied Surface Science*, vol. 503, pp. 144287–144295, 2020.
- [18] K. V. Özdokur, B. Bozkurt Çırak, Ç. Eden, M. Ahmad Boda, and Ç. Çırak, "Facile synthesis and enhanced photo-electrocatalytic performance of TiO<sub>2</sub> nanotube/g-C<sub>3</sub>N<sub>4</sub> composite catalyst by a novel synthesis approach," *Optik*, vol. 206, p. 164262, 2020.
- [19] S. Y. Janbandhu, A. Joshi, S. R. Munishwar, and R. S. Gedam, "CdS/TiO<sub>2</sub> heterojunction in glass matrix: synthesis, characterization, and application as an improved photocatalyst," *Applied Surface Science*, vol. 497, pp. 143758–143768, 2019.
- [20] J. Chen, M. Wang, J. Han, and R. Guo, "TiO<sub>2</sub> nanosheet/NiO nanorod hierarchical nanostructures: p-n heterojunctions towards efficient photocatalysis," *Journal of Colloid and Interface Science*, vol. 562, pp. 313–321, 2020.
- [21] Z. Guo, J. Wei, B. Zhang, M. Ruan, and Z. Liu, "Construction and photoelectrocatalytic performance of TiO<sub>2</sub>/BiVO<sub>4</sub> heterojunction modified with cobalt phosphate," *Journal of Alloys and Compounds*, vol. 821, pp. 153225–153234, 2020.
- [22] J. Jia, C. Jiang, X. Zhang et al., "Urea-modified carbon quantum dots as electron mediator decorated g-C<sub>3</sub>N<sub>4</sub>/WO<sub>3</sub> with enhanced visible-light photocatalytic activity and mechanism insight," *Applied Surface Science*, vol. 495, pp. 143524–142534, 2019.
- [23] M. Parthibavarman, M. Karthik, and S. Prabhakaran, "Facile and one step synthesis of WO<sub>3</sub> nanorods and nanosheets as an efficient photocatalyst and humidity sensing material," *Vacuum*, vol. 155, pp. 224–232, 2018.
- [24] K. M. Pan, K. N. Shan, S. Z. Wei et al., "Two-step alcohol-thermal synthesis and characterization of enhanced visible-light-active WO<sub>3</sub>-coated TiO<sub>2</sub> heterostructure," *Ceramics International*, vol. 46, no. 2, pp. 2101–2109, 2020.
- [25] Y. M. Hunge, A. A. Yadav, M. A. Mahadik et al., "Degradation of organic dyes using spray deposited nanocrystalline stratified WO<sub>3</sub>/TiO<sub>2</sub> photoelectrodes under sunlight illumination," *Optical Materials*, vol. 76, pp. 260–270, 2018.
- [26] H. Khan, M. G. Rigamonti, G. S. Patience, and D. C. Boffito, "Spray dried TiO<sub>2</sub>/WO<sub>3</sub> heterostructure for photocatalytic applications with residual activity in the dark," *Applied Catalysis B: Environmental*, vol. 226, pp. 311–323, 2018.
- [27] L. Zhang, J. Yin, K. Wei et al., "Fabrication of hierarchical SrTiO<sub>3</sub>@MoS<sub>2</sub> heterostructure nanofibers as efficient and low-cost electrocatalysts for hydrogen-evolution reactions," *Nanotechnology*, vol. 31, no. 20, p. 205604, 2020.
- [28] B. Su, K. Wang, N. Dong et al., "Biomorphic synthesis of long ZnO hollow fibers with porous walls," *Journal of Materials Processing Technology*, vol. 209, no. 8, pp. 4088–4092, 2009.
- [29] Y. J. Li, T. P. Cao, C. L. Shao, and L. M. Wei, "Preparation and photocatalytic properties of ZnO/PAN submicron composite fibers," *Chinese Journal of Inorganic Chemistry*, vol. 27, no. 7, pp. 1348–1352, 2011.
- [30] J. Hu, L. Wang, P. Zhang, C. Liang, and G. Shao, "Construction of solid-state Z-scheme carbon-modified TiO<sub>2</sub>/WO<sub>3</sub> nanofibers with enhanced photocatalytic hydrogen production," *Journal of Power Sources*, vol. 328, pp. 28–36, 2016.
- [31] H. Gao, P. Zhang, J. Zhao, Y. Zhang, J. Hu, and G. Shao, "Plasmon enhancement on photocatalytic hydrogen production over the Z-scheme photosynthetic heterojunction system," *Applied Catalysis B: Environmental*, vol. 210, pp. 297–305, 2017.
- [32] L. Soares and A. Alves, "Photocatalytic properties of TiO<sub>2</sub> and TiO<sub>2</sub>/WO<sub>3</sub> films applied as semiconductors in heterogeneous photocatalysis," *Materials Letters*, vol. 211, pp. 339–342, 2018.
- [33] C. Byrne, L. Moran, D. Hermosilla et al., "Effect of Cu doping on the anatase-to-rutile phase transition in TiO<sub>2</sub> photocatalysts: theory and experiments," *Applied Catalysis B: Environmental*, vol. 246, pp. 266–276, 2019.
- [34] Z. Ma, L. Deng, G. Fan, and Y. He, "Hydrothermal synthesis of p-C<sub>3</sub>N<sub>4</sub>/f-BiOBr composites with highly efficient degradation of methylene blue and tetracycline," *Spectrochimica Acta Part A: Molecular and Biomolecular Spectroscopy*, vol. 214, pp. 103–110, 2019.
- [35] C. Peng, B.-H. Yao, W. Zhang, J.-F. Niu, and J. Zhao, "Synthesis of CuAPTPP-TDI-TiO<sub>2</sub> conjugated microspheres and its photocatalytic activity," *Chinese Journal of Chemical Physics*, vol. 27, no. 2, pp. 200–208, 2014.
- [36] Z. S. Sun, Y. X. Chen, Q. Ke, Y. Yang, and J. Yuan, "Photocatalytic degradation of a cationic azo dye by TiO<sub>2</sub>/bentonite nanocomposite," *Journal of Photochemistry and Photobiology A: Chemistry*, vol. 149, no. 1-3, pp. 169–174, 2002.
- [37] L. Zhang, Q. Zhang, H. Xie et al., "Electrospun titania nanofibers segregated by graphene oxide for improved visible

- light photocatalysis," *Applied Catalysis B: Environmental*, vol. 201, pp. 470–478, 2017.
- [38] J. F. Moulder, W. F. Stickle, P. E. Sobol, K. D. Bomben, and J. Chastain, *Handbook of X-Ray Photoelectron Spectroscopy*, Perkin-Elmer Corporation, Waltham, MA, USA, 1992.
- [39] U. Diebold, "TiO<sub>2</sub> by XPS," *Surface Science Spectra*, vol. 4, no. 3, pp. 227–231, 1998.
- [40] O. Akhavan, "Lasting antibacterial activities of Ag-TiO<sub>2</sub>/Ag/a-TiO<sub>2</sub> nanocomposite thin film photocatalysts under solar light irradiation," *Journal of Colloid and Interface Science*, vol. 336, no. 1, pp. 117–124, 2009.
- [41] J. Singh, S. Sharma, S. Sharma, and R. C. Singh, "Effect of tungsten doping on structural and optical properties of rutile TiO<sub>2</sub> and band gap narrowing," *Optik*, vol. 182, pp. 538–547, 2019.
- [42] D. Tsukamoto, M. Ikeda, Y. Shiraishi et al., "Selective photocatalytic oxidation of alcohols to aldehydes in water by TiO<sub>2</sub> partially coated with WO<sub>3</sub>," *Chemistry-A European Journal*, vol. 17, no. 35, pp. 9816–9824, 2011.
- [43] S. Shenawi-Khalil, V. Uvarov, Y. Kraitsman, E. Menes, I. Popov, and Y. Sasson, "A new family of BiO(Cl<sub>x</sub>Br<sub>1-x</sub>) visible light sensitive photocatalysts," *Catalysis Communications*, vol. 12, no. 12, pp. 1136–1141, 2011.
- [44] M. R. S. Joice, T. M. David, and P. Wilson, "WO<sub>3</sub> nanorods supported on mesoporous TiO<sub>2</sub> nanotubes as one-dimensional nanocomposites for rapid degradation of methylene blue under visible light irradiation," *The Journal of Physical Chemistry C*, vol. 123, no. 45, pp. 27448–27464, 2019.
- [45] X. Zeng, Z. Wang, G. Wang et al., "Highly dispersed TiO<sub>2</sub> nanocrystals and WO<sub>3</sub> nanorods on reduced graphene oxide: Z-scheme photocatalysis system for accelerated photocatalytic water disinfection," *Applied Catalysis B: Environmental*, vol. 218, pp. 163–173, 2017.
- [46] Z. Ma, L. Hu, X. Li, L. Deng, G. Fan, and Y. He, "A novel nano-sized MoS<sub>2</sub> decorated Bi<sub>2</sub>O<sub>3</sub> heterojunction with enhanced photocatalytic performance for methylene blue and tetracycline degradation," *Ceramics International*, vol. 45, no. 13, pp. 15824–15833, 2019.